

On Microstructure Estimation Using Flatbed Scanners for Paper Surface Based Authentication

Runze Liu, *Student Member, IEEE* and Chau-Wai Wong, *Member, IEEE*

Abstract—Paper surfaces under the microscopic view are observed to be formed by intertwined wood fibers. Such structures of paper surfaces are unique from one location to another and are almost impossible to duplicate. Previous work used microscopic surface normals to characterize such intrinsic structures as a “fingerprint” of paper for security and forensic applications. In this work, we examine several key research questions of feature extraction in both scientific and engineering aspects to facilitate the deployment of paper surface-based authentication when flatbed scanners are used as the acquisition device. We analytically show that, under the unique optical setup of flatbed scanners, the specular reflection does not play a role in norm map estimation. We verify using a larger dataset than prior work that the scanner-acquired norm maps, although blurred, are consistent with those measured by confocal microscopes. We confirm that when choosing an authentication feature, high spatial-frequency subbands of the heightmap are more powerful than the norm map. Finally, we show that it is possible to empirically calculate the physical dimension of the paper patch needed to achieve a certain authentication performance in equal error rate (EER). We analytically show that $\log(\text{EER})$ is decreasing linearly in the edge length of a paper patch.

Index Terms—Authentication, physically unclonable, paper surface, microstructure, norm map, flatbed scanner, specular reflection

I. INTRODUCTION

When viewed under a microscope, mundane-seeming paper surfaces come to life, and a maze of intertwined wood fibers creates a complicated random jungle of structure [1]–[13]. The unique microscopic structure of the paper surface is physically unclonable and may be considered as a “fingerprint”, which can be used for protecting valuable merchandise such as drugs and wines and important documents such as birth certificates and checks. Two categories of methods have been used to capture such unique structure of paper surfaces for authentication, namely, the optical/visual feature approach and the physical feature approach.

The optical/visual approach relies on the visual appearance of the paper surface or handcrafted features derived from the visual appearance for paper identification. Buchanan et al. [3] used a laser scanner to capture the reflected intensity due to a moving focused line shined on the paper surfaces, and used cross-correlation of digitized intensity fluctuations for identification. As a proof-of-concept effort for paper-based identification, lasers achieved good performance, however, they are expensive and not ubiquitous to be used in

practical applications. Beekhof et al. [14] used macrolens-aided mobile phones to capture images of the rough paper surfaces. Minimum reference distance decoding and reference list decoding were used for the identification problem, with a huge reduction in complexity than classic minimum distance decoding while maintaining the performance. Sharma et al. [15] used paper speckles, i.e., the dark and bright spots on paper when illuminated by light, as a fingerprint for paper surface, where images of the paper surface were taken by a camera with aid of a microscope with a built-in LED. The Gabor transform was applied to the captured image, and a binary image was obtained by using the complex phase of the Gabor transform and zero thresholding. The fractional hamming distance was used to compare different binary images. Instead of analyzing the light reflected from paper surface, Toreini et al. [16] captured optical features of paper texture using the light transmitted through the paper and had satisfying authentication performance. However, it can only be applied in the scenarios that a sheet of paper is not glued to a surface and the paper is relatively transparent. For example, it is difficult to capture the transmissive light for a label stuck to a bottle or for stock paper packaging. The aforementioned methods for identifying paper surfaces are based on the optical/visual features, while their underlying physical features, such as the orientation of a microscopic surface, has been shown to possess greater discriminative power [4], [10].

The orientations of the microscopic surfaces of a paper patch may be quantified by the *norm map*, a collection of uniformly spaced surface normals projected to the xy -plane. Clarkson’s et al. [4] proposed a method for estimating a scaled version of the norm map of a paper patch by acquiring the paper in opposite orientations using a flatbed scanner assuming light reflection is fully diffuse. Instead of using a bulky flatbed scanner, Wong et al. [10] used a mobile camera to take multiple photos from different perspectives of a paper patch, estimating the norm map with the diffuse reflection model [17] and the camera geometry [18]. The estimated norm map was also verified by ground truth, a norm map acquired by a confocal microscope. Liu et al. [11] formulated two improved norm map estimators by taking into account the ambient light and cameras’ internal brightness and contrast adjustment processes. They also used estimated surface normals to reconstruct heightmaps/3D surfaces of paper patches and discovered that using the high spatial-frequency components of heightmaps as the authentication feature can achieve better performance than using the norm map.

Fig. 1 demonstrates two potential designs of real-world paper surface-based authentication systems, namely, a client-

R. Liu and C.-W. Wong are with the Department of Electrical and Computer Engineering and the Forensic Sciences Cluster, NC State University, Raleigh, NC 27695, USA. (e-mail: rliu10@ncsu.edu; chauwai.wong@ncsu.edu)

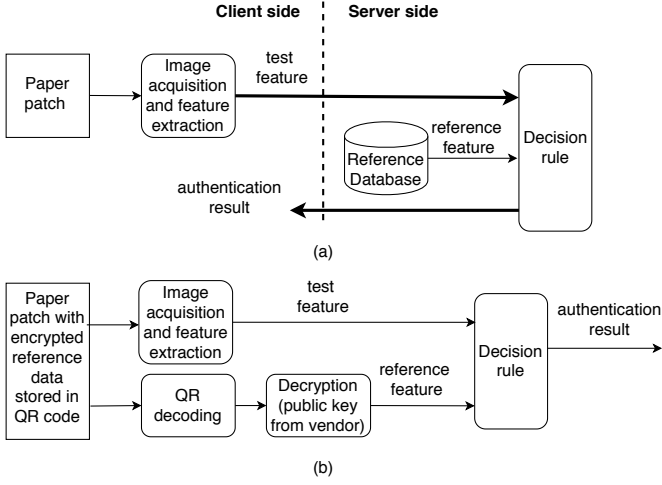


Fig. 1. Examples of paper surface-based authentication systems: (a) a client-server model, and (b) a local model. The thick arrows are encrypted communication links and the normal arrows are local communication links. The diagrams focus on the verification stage. The reference data are stored in the reference database or the QR code at an earlier enrollment stage.

server model and a local model. The authentication systems, by designating a small paper-based surface area for the purpose of authentication, can be used for protecting merchandise and important documents. For example, a customer can use a mobile phone with an app to obtain the feature of a drug package, and then compare it with the reference feature to verify the authenticity of the packaging. In the client-server model, a mobile phone as the client can acquire images of the paper patch, derive the test feature, and send the test feature to the server using a locally installed app. The server will search in its database whether the test feature matches an existing reference feature upon receiving it from the client. If the reference feature ID is also provided together with the test feature, the server can directly access the reference feature and use it for comparison, which can save the feature retrieval time and increase the authentication accuracy. The authentication result based on the matching outcome will be sent back to the client. In the client-server model, the communication channel between the two parties is protected by cryptographic protocols such as the transport layer security (TLS) to ensure the trustworthiness. In the local model, the encrypted communication is not needed but an additional QR code is used to store the reference feature protected by the public-key encryption. After decoding the QR code, the user will use the public-key from the vendor to unlock the reference feature. The test feature will be compared with the reference feature to generate the authentication result. Although in this local model the reference feature may be exposed to an untrusted user that tries to tap into the memory to intercept the decrypted reference feature, the attacker still needs to forge a paper patch from which the intercepted feature can be derived, which is impossible because the microstructure is physically unclonable.

To facilitate the deployment of paper surface-based authentication, we examine four key research questions of feature extraction in both scientific and engineering aspects when flatbed scanners are used as the acquisition device.

First, does ignoring the specular reflection have a destructive effect on the authentication performance? Prior approaches for estimating norm maps were based on the assumption that paper reflects the light in a fully diffuse way [4], [8]–[11]. In [4], it was argued that the fully diffuse assumption largely holds, but without justifications using experimental results or theoretical derivations. In [10], the strengths of diffuse versus the specular components were estimated to be about six to one, but the specular was not compensated in the norm map estimation. Since the specular reflection could also be practically observed for paper surfaces even by naked eyes, it is interesting to investigate whether explicitly taking the specular reflection into the estimator design may improve the accuracy. Second, does the estimated normal vector resemble the real quantity with physical interpretations? Prior work in [10] with a small dataset shows that norm map acquired by scanners are consistent with those measured by confocal microscopes. In this work, we use a confocal dataset of one order of magnitude larger to obtain a more confident conclusion and extend the inquiry into scanner’s blurring effect. Third, can feature engineering on the estimated normal vectors yield higher authentication performance? The result in [11] demonstrated that the heightmap and its higher-frequency subbands as features outperform norm maps for the mobile cameras. We investigate whether a similar conclusion can be drawn for flatbed scanners. Fourth, we also study how the paper patch size affects authentication performance and investigate the justification for digitizing resolutions for paper patches.

We summarize the contributions of this paper compared to previous work [10], [11] in both scientific and engineering aspects. The scientific contributions are as follows:

- We prove mathematically that the effect of the specular reflection can be ignored because of the unique imaging setup of flatbed scanners (but such result is not true for the camera setup);
- We investigate quantitatively on the performance drop due to the existence of blurring effect in the scanner, and use a one order of magnitude larger dataset than that of [10] to confirm that scanners can capture meaningful physical quantities of paper surfaces;

And the engineering contributions are as follows:

- We justify and give a guide to the choices for paper patch size and resolution with mathematical and experimental results, and investigate quantitatively on the performance drop due to spatial registration error;
- We confirm that using the heightmap as the feature proposed in [11] is also more discriminative than using the norm map for the flatbed scanners use case.

The rest of the paper is organized as follows. In Section II, we give some background reviews. In Section III, we analytically investigate the effect of specular reflection in the optical setup of flatbed scanners. In Section IV, we investigate the consistency between estimated norm maps from scanner and confocal microscope with a focus on the blurring effect. In Section V, we examine the performance of physical features such as the heightmap and their subbands. In Section VI, we

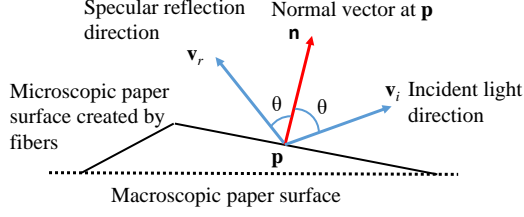


Fig. 2. A microscopic view of a paper surface with annotated quantities related to light reflection at location \mathbf{p} . The vectors are all unit vectors.

investigate the digitizing resolution and the size of paper patch needed for achieving a certain performance level. Section VII concludes the paper.

II. BACKGROUND AND PRELIMINARIES

Symbol conventions are as follows. Nonitalic bold letters denote vectors and all vectors in this paper are column vectors. For example, $\mathbf{n} = (n_x, n_y, n_z)$ defines a column vector with elements n_x , n_y and n_z .

A. Difference-of-Gaussians (DoG) Representation

In DoG representation [19], [20] representation, the n th level subband is obtained by taking differences of the Gaussian-blurred matrix of numbers as follows:

$$\mathbf{L}_n = \mathbf{G}_n - \mathbf{G}_{n+1}, \quad n = 1, \dots, N \quad (1)$$

where \mathbf{G}_1 is defined to be the original matrix, $\mathbf{G}_{N+1} = 0$, and \mathbf{G}_n , $n = 2, \dots, N$, is the result of blurring the original matrix by a Gaussian filter with standard deviation σ^{n-1} , where $\sigma > 1$. The DoG representation of a matrix allows us to investigate the different spatial-frequency subbands of the matrix, as shown in Section V-B and the supplementary document.

B. Generalized Light Reflection Model

Fig. 2 illustrates a microscopic portion of a paper surface containing small surfaces that usually orient differently than the macroscopic paper surface. Pick an arbitrary location $\mathbf{p} \in \mathbb{R}^2$ on the surface and assume both diffuse and specular reflection types, the perceived intensity l_r for a sensor or an eye at a fixed distance away from \mathbf{p} may be written as the following generalized light reflection model, i.e., Phong shading model without the ambient light [17]:

$$l_r = \frac{l}{\|\mathbf{o} - \mathbf{p}\|^2} \left\{ w_d \cdot (\mathbf{n}^T \mathbf{v}_i)^+ + w_s \cdot (\mathbf{v}_c^T \mathbf{v}_r)^{k_e} \right\}, \quad (2)$$

where $\mathbf{n} = (n_x, n_y, n_z)$ is the microscopic normal direction of the paper surface at location \mathbf{p} , $\mathbf{o} = (o_x, o_y, o_z)$ is the position of the light source, $\mathbf{v}_i = (\mathbf{o} - \mathbf{p}) / \|\mathbf{o} - \mathbf{p}\|$ is the incident light direction, l is the strength of the light, $1/\|\mathbf{o} - \mathbf{p}\|^2$ is a light-strength discounting factor as the received energy per unit area from a point light source is inversely proportional to the squared distance. $x^+ = \max(0, x)$, and $k_e > 0$ controls the gloss level of the surface. w_d and w_s are the weights for diffuse and specular components, and they have taken into account the effect of a constant surface albedo and other

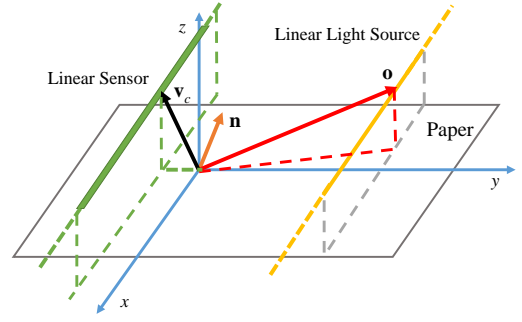


Fig. 3. Configuration of the optical system of a flatbed scanner for scanning a paper sheet. The point of interest is located at the origin. The microscopic surface normal, \mathbf{n} , the camera/sensor direction, \mathbf{v}_c , and the location of one point on the linear light, \mathbf{o} , are shown.

scaling factors. \mathbf{v}_c is the camera's/sensor's direction, and \mathbf{v}_r is the specular reflection direction which can be written in terms of the incident light direction \mathbf{v}_i and the normal vector \mathbf{n} , i.e., $\mathbf{v}_r = (2\mathbf{n}\mathbf{n}^T - \mathbf{I})\mathbf{v}_i$, where \mathbf{I} is the identity matrix. All \mathbf{n} , \mathbf{v}_i , \mathbf{v}_c , and \mathbf{v}_r are unit-length column vectors.

C. Norm Map Estimation Using Photometric Stereo

Surface normal is a vector perpendicular to the tangent plane at a location of the surface, and normal vector field is a collection of 3D surface normals over a 2D grid. Norm map is the normal vector field projected onto the xy -plane, which is a 2D vector field. Norm map has been shown to be a powerful discriminative feature for paper surface [4], [10], [11].

The state-of-the-art method for estimating norm maps of paper surfaces using commodity flatbed scanners [4], [8]–[11] is described as follows. We assume the paper to be scanned is placed on the xy -plane passing through the origin as shown in Fig. 3. Without loss of generality, we assume that the point of interest is located at the origin. A linear light source is positioned in parallel with the x -axis and moving along the y -axis. We denote a specific location on the linear light source as \mathbf{o} and the incident light direction is therefore $\mathbf{v}_i = (o_x, o_y, o_z) / \|(o_x, o_y, o_z)\|$. Since the light source is very close to the paper surface, the linear light source appears to a point on the paper infinitely long in the x -direction.

Under the fully diffuse model, the intensity I of the reflected light of the point placed at the origin under the linear light of a flatbed scanner is a superposition of all rays diffusely reflected originating from the light source located at $\mathbf{o} = (o_x, o_y, o_z)$ for $o_x \in [-a, b]$, where $-a$ and b are the x -coordinates of the two ends of the linear light source and assume $0 < a < b$:

$$I = \int_{-a}^b l_r \, do_x \approx l \cdot w_d \int_{-a}^a \mathbf{n}^T \frac{(o_x, o_y, o_z)}{\|(o_x, o_y, o_z)\|^3} \, do_x, \quad (3)$$

where the approximation makes use the fact that the intensity of the point of interest contributed by the far portion $o_x \in (a, b]$ of the linear light source is very small, namely, $\int_a^b \mathbf{n}^T \mathbf{o} / \|\mathbf{o}\|^3 \, do_x \approx 0$.

In [4], [8]–[11], images acquired using a scanner from two opposite directions are used to estimate x - or y -component of norm map. Two images, I_{0° and I_{180° , are obtained when

paper is orientated at 0° and 180° on the xy -plane when being scanned. For a pixel of interest on the paper surface, the normal vector is \mathbf{n} , and a specific location on the light source is $\mathbf{o} = (o_x, o_y, o_z)$. When scanning the paper at 180° , it is equivalent that for the pixel of interest, the normal vector remains the same, while flipping the lights y coordinate, namely, changing the specific location on the light source into $\mathbf{o}' = (o_x, -o_y, o_z)$.¹ Their difference, $I_{0^\circ} - I_{180^\circ}$, can be shown to be in proportional to the y -component of the norm map, n_y , and therefore can be used as an estimator for n_y [4]:

$$I_{0^\circ} - I_{180^\circ} = l \cdot w_d \int_{-a}^a \mathbf{n}^T \frac{\mathbf{o} - \mathbf{o}'}{\|(\mathbf{o}_x, o_y, o_z)\|^3} do_x = s n_y, \quad (4)$$

where $s = 2l \cdot w_d o_y \int_{-a}^a \|\mathbf{o}\|^{-3} do_x$ is a constant. The x -component of the normal vector, n_x , can be estimated similarly using $I_{90^\circ} - I_{270^\circ}$.

III. CANCELLATION OF SPECULAR COMPONENTS UNDER FLATBED SCANNER GEOMETRY

The state-of-the-art norm map estimation method [4], [10] reviewed in Section II-C assumes that paper surfaces reflect light in a fully diffuse way. However, if one observes carefully a paper patch at a close distance under a strong light while constantly changing the observation angle, he/she may observe some discrete spots with significant intensity fluctuation. These discrete spots are not fully diffuse, since perceived intensity due to diffuse reflected light should not depend on the location of eye/sensor. For a spot dominated by the specular reflection, the perceived intensity could be much stronger or weaker than its neighboring spots dominated by the diffuse reflection. This is because the intensity given by the specular reflection has a different cause that depends on the angle between the directions of the eye and the reflected light, namely, $\arccos(\mathbf{v}_c^T \mathbf{v}_r)$. For these spots with a specular reflection component, the estimation of the normal vector may be very different from the true value if the specular component is neglected. To demonstrate this phenomenon, we contrast in Fig. 4 real photos captured by a mobile camera and their corresponding synthesized versions by only considering the diffuse component. The photos were captured in different camera orientations with different incident light directions. The synthesized versions were generated by first estimating the normal vector field assuming the fully diffuse Model 2 proposed in [11], and then rendering diffuse reflection images. It is revealed in Fig. 4 that the real photos in the first row have more highlights than the synthesized images in the second row that could be due to the specular reflection. We circled some locations of high contrast in real photos that are surrounded by dark pixels. The corresponding locations in synthesized images do not have such high contrast.

We have demonstrated that in general geometry setups for capturing paper surfaces such as using cameras, there will be high-contrast spots in the captured images due to the specular reflection component. Blindly ignoring specular reflections in

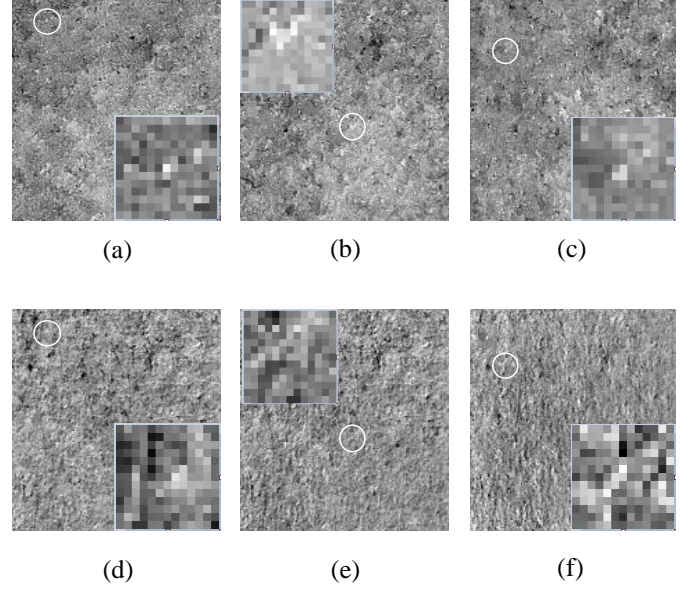


Fig. 4. (a)–(c) Photos of a paper patch captured by a mobile camera from different angles with flashlight. (d)–(f) Synthetic images that consider only the diffuse reflection. The real photos have high-contrast spots that may be caused by specular reflection, whereas their contrast in respective synthetic images is much lower. Vertical two images form a pair to be compared, with circles highlighting collocated spots for visual comparison. The zoomed in versions in the circled areas are put in the corners of the images. (All pictures have undergone perspective transform, detrending, and contrast enhancement to better illustrate the idea.)

modeling and estimation may lead to imprecise norm map estimates. Next, we show analytically that, for the flatbed scanner geometry, the image subtraction approach remains a precise estimator even if specular reflection is taken into consideration. Using the generalized light reflection model (2) that contains the specular reflection term, the reflected intensity under a scanner's linear light becomes:

$$\begin{aligned} I &= \int_{-a}^a l_r do_x = l \int_{-a}^a (w_d \mathbf{n}^T \mathbf{v}_i + w_s \mathbf{v}_c^T \mathbf{v}_r) \frac{1}{\|\mathbf{o}\|^2} do_x \\ &= l \int_{-a}^a \left(w_d \mathbf{n}^T + w_s \mathbf{v}_c^T (2\mathbf{n}\mathbf{n}^T - \mathbf{I}) \right) \mathbf{v}_i \frac{1}{\|\mathbf{o}\|^2} do_x. \end{aligned} \quad (5)$$

Note that we set $(\mathbf{n}^T \mathbf{v}_i)^+ = \mathbf{n}^T \mathbf{v}_i$ when invoking (2) since the angle between \mathbf{n} and \mathbf{v}_i are rarely greater than 90° . We set $k_e = 1$ to capture the dominating linear relationship while ignoring the higher-order terms for analytic tractability.

When scanning the paper in two opposite directions, a more natural and direct modeling approach is not to flip the light's y coordinate as proposed in [4] and reviewed in Section II-C of this paper; instead, following the illustration of Fig. 3, we should capture the 180° rotation operation in the xy -plane resulting $\mathbf{n}' = (-n_x, -n_y, n_z)$ while leaving the incident light direction \mathbf{v}_i and the camera direction \mathbf{v}_c unchanged. Following the traditional procedure of subtracting one scanned image from another, we obtain:

$$\begin{aligned} I_{0^\circ} - I_{180^\circ} &= s n_y \\ &+ 2l \int_{-a}^a \left(w_s \mathbf{v}_c^T (\mathbf{n}\mathbf{n}^T - \mathbf{n}'\mathbf{n}'^T) \mathbf{v}_i \right) \frac{1}{\|\mathbf{o}\|^2} do_x. \end{aligned} \quad (6)$$

The x -component of camera direction $v_{cx} = 0$ since the camera/sensor in the scanner catches the light that is parallel

¹Note that this equivalence by flipping the y coordinate of the light is only valid for the fully diffuse model. In Section III that incorporates the specular component, we do not use this equivalence.

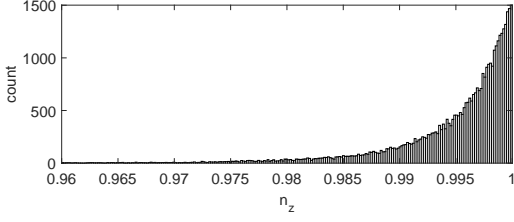


Fig. 5. A histogram for the z -component of the normal vector field of a 2/3-by-2/3 inch² paper patch from confocal laser scanning microscope Keyence VKx1100 digitized at a spatial resolution of 5.38 μm .

to yz -plane, and $n_z \approx 1$ since normal vectors are close to pointing straight up, as is revealed by Fig. 5—a histogram for n_z obtained from measurements using a confocal microscope. Substituting $\mathbf{v}_c = (v_{cx}, v_{cy}, v_{cz})$, $\mathbf{v}_i = \mathbf{o}/\|\mathbf{o}\|$ and

$$\mathbf{nn}^T - \mathbf{n}'\mathbf{n}'^T = \begin{bmatrix} 0 & 0 & 2n_x n_z \\ 0 & 0 & 2n_y n_z \\ 2n_x n_z & 2n_y n_z & 0 \end{bmatrix} \text{ into (6), we obtain:}$$

$$I_{0^\circ} - I_{180^\circ} = sn_y + 4l \int_{-a}^a w_s(v_{cz}n_x n_z, v_{cz}n_y n_z, \quad (7a)$$

$$v_{cx}n_x n_z + v_{cy}n_y n_z)^T (o_x, o_y, o_z) \|\mathbf{o}\|^{-3} do_x \\ = sn_y + 2s'n_z \left\{ n_y \left[v_{cz} + v_{cy}o_z/o_y \right] + n_x v_{cx}o_z/o_y \right\} \quad (7b)$$

$$\approx [s + 2(v_{cz} + v_{cy}o_z/o_y)s']n_y \quad (7c)$$

where $s' = 2l \cdot w_s o_y \int_{-a}^a \|\mathbf{o}\|^{-3} do_x$. We followed the procedure outlined in [10] to generate normal vectors from the heightmap acquired by a confocal microscope. Note that o_z and o_y are device-specific constants since the distance from the light source to the point being captured in xz -plane is fixed by the design of scanner geometry. The final result in (7c) reveals that even though the specular reflection is taken into account, the traditional estimator is still linear in n_y due to the unique imaging setup by flatbed scanners. This would not be possible if v_{cx} were not zero since both n_x and o_z are usually nonzero.

Note that the result that the specular component does not play a role is largely contributed by the approximately symmetric integration bound from $-a$ to a demonstrated in (3), which is in turn guaranteed by the fact that the linear light is very close to the paper to be scanned in the z direction. The result we obtained in this section does not apply to more general geometric setups such as using mobile cameras discussed in other literature [5]–[7], [9]–[11]. This result also justifies the use of a flatbed scanner to obtain norm maps for surfaces other than paper that contain stronger specular components.

IV. SCANNER AND CONFOCAL CONSISTENCY

A preliminary study was reported in Section VII.C of [10] examining whether the norm map estimated from scanner acquired images are consistent with the ground truth, i.e., the norm map measured by the confocal microscope. The overall correlation between the scanner estimates and the reference was 0.28 (we reproduced this number in Table I for easy reference and comparison), indicating that the estimation, even though not that precise, was indeed related to the ground

TABLE I
COMPARISON OF PERFORMANCE OF VARIOUS FEATURES WHEN TEST DATA FROM SCANNER CORRECTLY MATCH WITH REFERENCE DATA FROM CONFOCAL MICROSCOPE

Feature	Correlation
<i>Norm Map Based:</i>	
Raw (dataset of [10])	0.28
Raw (new dataset)	0.357 (x), 0.301 (y)
Deblurred (new dataset)	0.442 (x), 0.396 (y)
<i>Heightmap Based:</i>	
Reconstructed heightmap	0.358
Detrended reconstructed heightmap	0.499
Third-highest spatial-frequency subband	0.714

truth. However, in [10], only one physical paper patch was investigated. In this paper, we extended the inquiry of [10] by using a confocal collected dataset of one order of magnitude larger and investigate the blurring issue, aiming to confirm with higher confidence that the scanner estimated norm map are meaningful physical quantities and to gain better understandings about the characteristics of the scanner estimated norm maps.

A. Dataset Collection

In this paper, we created a new dataset of paper surfaces that will be made publicly available on the authors' websites after the publication of this paper. We collected data for 9 different paper patches of size $\frac{2}{3}$ -by- $\frac{2}{3}$ inch² using flatbed scanners and a confocal microscope. The patches are from the same sheet of ordinary office printing paper. This is a more difficult case than the case where paper patches are obtained from different sheets of printing papers because the paper patches from the same sheet exhibit less variations due to the same manufacturing condition, time, and raw materials used. The papers with printing are not considered since we aim to derive the intrinsic physical features caused by the intertwined wood fibers on paper surface. Four out of nine paper patches were stuck to a microscope glass slide to create a rigid and consistently flat surface. A card stock was put between the paper and the glass slide to block any light from the backside of the paper. The other five paper patches were not stuck to anything. These two different setups mimic the conditions of patches in real-world scenarios.

Data related to the flatbed scanner include scanner acquired images. For image acquisition, we used Canon CanoScan LiDE 110 flatbed scanner to acquire each patch from four orientations, i.e., 0° , 90° , 180° and 270° , and repeat such process three times for each physical patch to obtain three norm maps. The norm maps were estimated by taking the difference of images scanned in opposite directions, which is based on the fully diffuse model since we have analytically proved the specular component can be neglected in the optical setup of a scanner in Section III. Then we repeated the image acquisition process by using two other consumer-grade flatbed scanners that are the most popular on Amazon.com as of the summer of 2019, CanoScan LiDE 300, and Epson

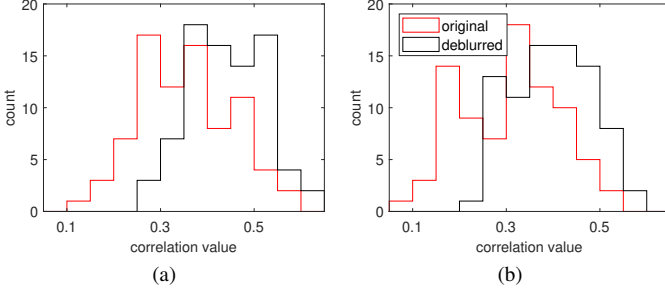


Fig. 6. Histograms of correlation values between (a) x - or (b) y -component of norm maps estimated from scanner and confocal measurements. The averaged correlation increased from 0.357 to 0.442 for the x -component and from 0.301 to 0.396 for the y -component after deblurring.

Perfection V39. Using the three scanners, we obtain a total of nine norm maps for each paper patch. We resized the acquired patch images to 200-by-200 pixels. Data related to the confocal microscope include heightmaps of paper surfaces and norm maps derived from heightmaps that are accurate enough to be considered as ground truth. We used a Keyence VKx1100 confocal microscope with a 404 nm violet laser source to obtain heightmaps of paper patches. We followed the procedure in [10] to derive a 200-by-200 norm map from the heightmap for each paper patch: We estimated the normal vector for a pixel of interest by fitting a plane to the corresponding height values located in the z direction. The resolution in z direction of the heightmap used in this data acquisition was 0.1 nm, which is much higher than 6 μm used in [10] and can therefore provide more accurate aggregated results for confocal generated norm maps. Due to the optical principles of confocal microscopy, the confocal norm map is accurate enough to be considered as the ground truth.

B. Initial Consistency Verification

We evaluated the consistency of the scanner estimated norm maps to the confocal measurements on the newly collected dataset following the same procedure as in [10]. For each paper patch, we calculated the correlation between x -/ y -component of the nine norm maps obtained from the scanners and the ground-truth norm map from confocal microscope. Histograms of the correlation values are shown using the “original” legend of Fig. 6. The averaged correlation is 0.357 for x -component of norm map and 0.301 for y -component, as summarized in Table I, with the sample standard deviation 0.10 and 0.11, respectively. The averaged correlation values are close to the result, 0.28, reported in [10]. Our experimental results by using nine times of paper patches confirm with higher confidence that the scanner estimated norm maps are meaningful physical quantities.

C. Consistency Verification by Compensating Blurring

Although the previous subsection confirms that scanner norm maps are meaningful estimates of physical quantities, the correlation slightly greater than 0.3 implies that there are still non-negligible factors contributing to the inconsistency. One such factor may be spatial blurring. In this subsection,

we investigate the blurring effect due to the imaging pipeline of flatbed scanners on the accuracy of estimated norm maps. Images captured by flatbed scanners may be blurred due to out of focus, sensor/light/scanning platform motion, and the blooming effect of CCD sensors. Norm maps derived from blurred scanned images will therefore be a blurred version of the ground-truth norm maps. Below, we examine whether deblurring is possible with the help of confocal norm maps and investigate the characteristics of blurring filters.

1) *Deblurred Norm Map*: We explore using confocal norm maps to assist the deblurring process and evaluate the quality of deblurred norm maps. We denote the norm map from the confocal measurement as \mathbf{C} , and the norm map estimated by subtracting the two images scanned in opposite directions as \mathbf{S} . We model the relation between the ground truth \mathbf{C} and the scanner norm map considered to be blurred using the following linear model:

$$\mathbf{C} = \mathbf{H}_{\text{deblur}} * \mathbf{S} + \mathbf{e}, \quad (8)$$

where $\mathbf{H}_{\text{deblur}}$ is a linear spatial invariant (LSI) deblurring filter, \mathbf{e} is an error term, and $*$ is the 2D convolution operator. We create separate models for x - and y -components of a norm map and for each paper patch. Regarding the size of the deblurring filter, we empirically set the dimension such that the pixels with significant contributions to the convolutional result will be retained. Specifically, we use an oversized filter, i.e., 25-by-25, to preliminarily estimate filter coefficients when the filter dimension is not significantly constrained. Since it is a deblurring filter, the coefficient of the pixel in the center must dominate in magnitude when compared to other pixels. We observe that most coefficients with magnitude greater than 10% of that of the centering pixel are located in the centering 7-by-7 area. Hence, we will use 7-by-7 as the size to formally estimate the deblurring filters as follows.

To avoid model overfitting, we estimate the deblurring filter $\mathbf{H}_{\text{deblur}}$ using cross-validation with the cost function in the ridge regression form shown as follows:

$$\min_{\mathbf{H}_{\text{deblur}}} \|\mathbf{C} - \mathbf{H}_{\text{deblur}} * \mathbf{S}\|_F^2 + \lambda \|\mathbf{H}_{\text{deblur}}\|_F^2, \quad (9)$$

where $\|\cdot\|_F$ is the Frobenius norm and λ is a regularization parameter controlling model complexity. With norm map of size 200-by-200, the filter size to be 7-by-7, there are 34596 data points to solve for $\mathbf{H}_{\text{deblur}}$. We first use 10-fold cross-validation to find the regularization parameter that minimizes the cross-validation error. We then apply one standard error rule to choose an updated regularization parameter that corresponds to the most parsimonious model and use the coefficients at this time as the final estimate for the deblurring filter, $\hat{\mathbf{H}}_{\text{deblur}}$.

We use the trained filter $\hat{\mathbf{H}}_{\text{deblur}}$ to derive the deblurred norm map, $\hat{\mathbf{C}} = \hat{\mathbf{H}}_{\text{deblur}} * \mathbf{S}$, and compare it with the ground truth, the confocal norm map \mathbf{C} . The histograms of the correlation values between \mathbf{C} and $\hat{\mathbf{C}}$ in x - and y -directions are shown using the “deblurred” legend of Figs. 6(a) and (b), respectively. Due to deblurring, the averaged correlations increased from 0.357 to 0.442 for the x -component and from 0.301 to 0.396 for the y -component. Their sample standard deviations also decreased to 0.08 and 0.08, respectively. The increased correlations and decreased standard deviations after

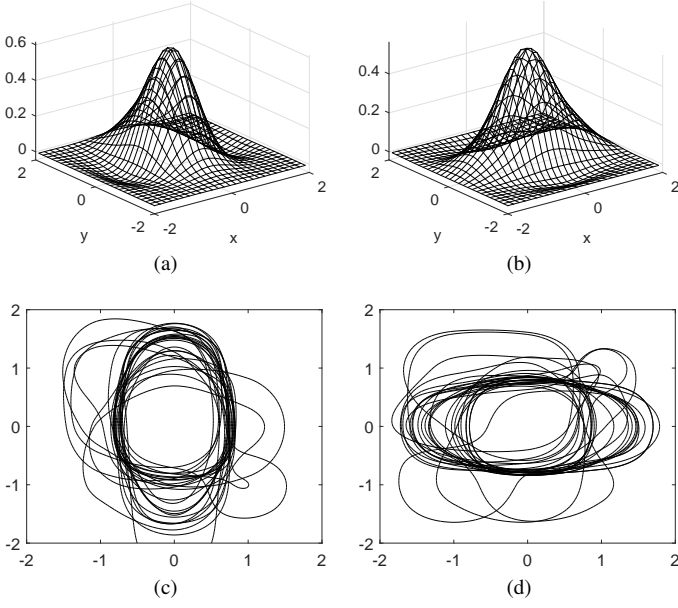


Fig. 7. Typical 3D mesh for the blurring filter for (a) x - or (b) y -component of the norm map of a paper patch. We also overlay the contour graphs (one contour per contour graph) for all nine paper patches to illustrate the shape of blurring filters for (c) x - or (d) y -component of norm maps. The blurring filters for x -component of norm maps have larger variance in y -direction and the blurring filters for y -component of norm maps have larger variance in x -direction.

deblurring indicates that blurring is a factor to the lowered quality of scanner estimated norm maps. It is also noted that, in light of the non-negligible but limited improvement of the correlation due to deblurring, more investigations are needed to reveal other factors limiting the accuracy of the scanner norm maps. In the practical authentication system in Section V-C, we do not apply deblurring due to the limited improvement of correlation.

2) *Shape of Blurring Filter*: It is also interesting to estimate the blurring filter to directly reveal the characteristic of blurring. First, we use a nonparametric approach to determine the shape of the blurring filter, which can avoid bias due to imposing a parametric model that may potentially cause mismatch. We estimated a 7-by-7 LSI filter \mathbf{H}_{blur} such that $\|\mathbf{S} - \mathbf{H}_{\text{blur}} * \mathbf{C}\|_F^2$ was minimized. Since the coefficients in the blurring filter should all be non-negative, we estimated the blurring filter \mathbf{H}_{blur} using non-negative least-squares. Because the blurring filter has a lowpass nature and is an inverse filter of the deblurring filter, even a filter smaller than 7-by-7 should be sufficient to adequately capture the blurring effect.

After obtaining an estimate of the blurring filter defined on a 7-by-7 grid, we interpolated the filter spatially and drew the 3D meshes and contours/level curves to visualize its shape. Figs. 7(a) and (b) depict two typical 3D meshes for blurring filters derived from the x - and y - components of the norm map of one paper patch, respectively. Figs. 7(c) and (d) show one contour per filter for all paper patches used in our experiments. The shapes of the contours reveal that the blurring filters for x -component of norm maps have larger spread in y -direction and the blurring filters for y -component of norm maps have larger spread in x -direction. The shapes of the contours are similar, so different scanners have similar blurring effects.

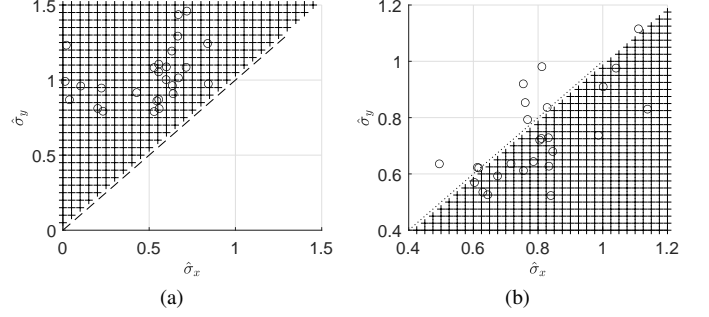


Fig. 8. Scatter plot of $(\hat{\sigma}_x, \hat{\sigma}_y)$ for the blurring filters of (a) x - or (b) y -component of the norm maps for all nine paper patches. In x -component of norm map the variance in x -direction is smaller, and in y -component of norm map the variance in y -direction is in general smaller, as illustrated through the shaded regions.

Since the blurring filters are close to bell-shaped, we further obtain a quantitative description of the spread for the blurring filters using parametric Gaussian filters. Let us assume a blurring filter that is generated by discretizing and normalizing a separable bivariate Gaussian function on a 7-by-7 grid. The bivariate Gaussian is parameterized by $\mu_x, \mu_y, \sigma_x, \sigma_y$, where (μ_x, μ_y) describes the location of the filter, σ_x and σ_y are the standard deviations of the Gaussian filter in x and y directions. We assume the Gaussian to be separable based on the fact that blurring in the x and y directions have different causes due to the geometry of the flatbed scanner, and the observations from Fig. 7 that nonparametrically estimated filters' contours are oriented horizontally or vertically. We estimate $\mathbf{H}_{\text{blur}}^{\text{Gaussian}} = \mathbf{G}(\mu_x, \mu_y, \sigma_x, \sigma_y)$ by solving the following minimization problem:

$$\min_{\mu_x, \mu_y, \sigma_x, \sigma_y, \theta} \|\mathbf{S} - \mathbf{G}(\mu_x, \mu_y, \sigma_x, \sigma_y) * \mathbf{C}\|_F^2. \quad (10)$$

Since this problem is nonconvex, we numerically solve it with the following starting point configurations by taking into consideration the nonparametric results summarized in Fig. 7: $\sigma_x = \sigma_y = 1$, and μ_x, μ_y uniformly randomly drawn from -0.5 to 0.5 . The estimated standard deviations in x - and y -components of the norm maps for different paper patches are shown in Fig. 8, which are consistent with the results in Fig. 7.

The results of parametric Gaussian filters confirmed the following patterns obtained from nonparametric least-squares method: i) the variance in x -direction is smaller for x -component of norm map, and ii) the variance in y -direction is smaller for y -component of norm map. Note that a smaller variance indicates a weaker blurring effect. This phenomenon could be explained by the unique optical setup of flatbed scanners. The y -component of norm map of the paper patch is estimated by taking the differences of two images scanned in the opposite directions along y -direction. During the scan, the linear sensor bar in the scanner is parallel to the x -axis, as shown in Fig. 3. The optical blurring along the direction of the linear light and the CCD blooming effect may result in more blurring along the x -direction, making the variance in x -direction larger in the y -component of norm map.

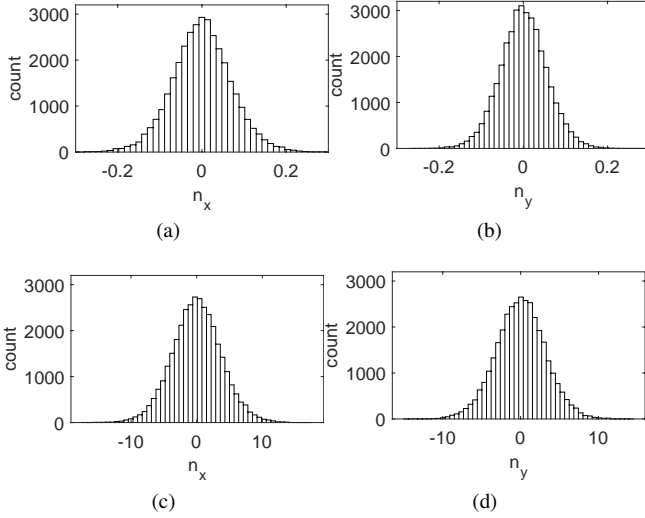


Fig. 9. Histograms for (a) x - and (b) y -components of norm map from confocal microscope. Histograms for (c) x - and (d) y -components of norm map from scanner. Note that the components calculated from scanner are off by an unknown scaling factor. The distributions are Gaussian-like and roughly centered around zero.

V. HEIGHTMAP AS A DISCRIMINATIVE FEATURE

Although the norm map has been shown to be a powerful discriminative feature [4], [10], when it is used in a practical authentication system, it is desirable to further increase the discriminative power to ensure a better performance. Previous work in [11] used the estimated norm map to reconstruct the 3D surface/heightmap and discovered that high-frequency subbands of reconstructed heightmap are more powerful than the norm map in describing the uniqueness of a physical surface. The result in [11] was demonstrated for mobile cameras and in this section, we investigate whether a similar conclusion can be drawn for flatbed scanners.

A. Z-Component Estimation From Norm Map

In this subsection, we propose an estimator for the z -component of normal vector field based on a known norm map for surface reconstruction. Surface reconstruction in general requires a normal vector field containing for each location a 3-D description about the orientation [17], [21]. However, using images acquired by scanners and the estimation technique presented in Section III, only the norm map, i.e., the scaled versions of the x - and y -components of the normal vector field, $(n_x^{(s)}, n_y^{(s)})$, are available. The authors of [11] proposed a distribution matching approach to estimate scalars α_x and α_y that correctly normalizes the norm map so that the z -component can be calculated using $\hat{n}_z = \left[1 - (n_x^{(s)}/\hat{\alpha}_x)^2 - (n_y^{(s)}/\hat{\alpha}_y)^2\right]^{1/2}$, where the quantities with hats are the corresponding estimated values. The distribution matching approach finds the best $\hat{\alpha}_x$ and $\hat{\alpha}_y$ such that the standard deviations of $n_x^{(s)}/\hat{\alpha}_x$ and $n_y^{(s)}/\hat{\alpha}_y$ will match those of the confocal. However, details for obtaining $\hat{\alpha}_x$ and $\hat{\alpha}_y$ were not given. Below, we justify the approach proposed in [11] and propose a least-squares formula for estimating a shared scalar α for both directions. We first examine the real data to support subsequent model design. We show histograms

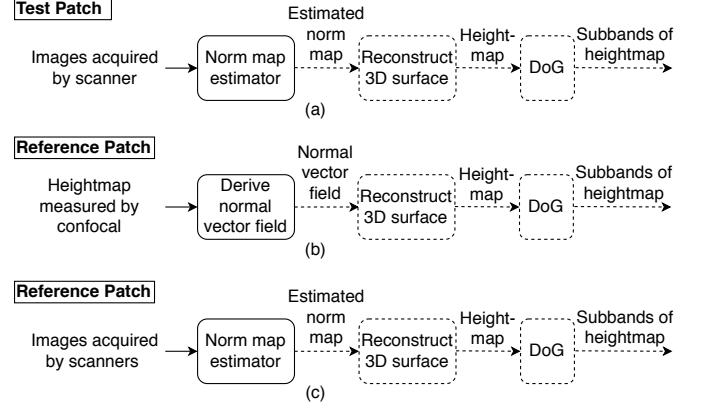


Fig. 10. (a) Block diagram for obtaining features from test patch using images acquired by flatbed scanner. Block diagrams for obtaining features from reference patch using (b) measurement from confocal microscope, or (c) images acquired by flatbed scanner. The norm map, the heightmap, or the subbands can be used as discriminative features. The blocks/processes with dashed boundaries should be ignored when their inputs are used as features.

for the x -, y -, and z -components of the normal vector field in Figs. 9(a), 9(b), and 5(a), respectively. From the histograms, we can see that normal vectors are on average pointing straight up due to large n_z and are without obvious bias in both x - and y -directions. The distributions are Gaussian-like and centered around zero. We also plot the histograms for x - and y -components of norm map that are scaled. We observe that they are similarly distributed as those from confocal but scaled, centering around 0. The above observation on the real data implies that a scaling relation is enough to connect the norm map to the first two components of normal vector field, namely, $n_x^{(c)}$ and $n_y^{(c)}$. Since the x - and y -components of the norm map are obtained by the same scanning process with the only difference in scanning directions, a shared multiplicative scalar should be used for both dimensions, namely,

$$(n_x^{(s)}, n_y^{(s)}) \approx \alpha \cdot (n_x^{(c)}, n_y^{(c)}), \quad (11a)$$

$$(\sigma_x^{(s)}, \sigma_y^{(s)}) \approx \alpha \cdot (\sigma_x^{(c)}, \sigma_y^{(c)}), \quad (11b)$$

where (11b) was obtained by considering α as a constant and other components in (11a) as random variables, and by applying the variance operation to both sides of (11a). Estimating α using least-squares from (11b), we obtain

$$\hat{\alpha} = (\sigma_x^{(s)}\sigma_x^{(c)} + \sigma_y^{(s)}\sigma_y^{(c)}) / (\sigma_x^{(c)2} + \sigma_y^{(c)2}), \quad (12)$$

which blends in the scaling effect in both directions. This formula allows the calculation of a scalar for a scanner norm map by using merely two summary statistics of paper surface, $\sigma_x^{(c)}$ and $\sigma_y^{(c)}$, that are determined by physical characteristics of papers and are stable numbers for papers of the same type [22].

B. Heightmap and Subbands as Discriminative Features

In [11], the authors have shown experimentally for mobile cameras acquired images that the high frequency subbands have been proved to be powerful discriminative features for authentication. In this work, we validate the method of [11]

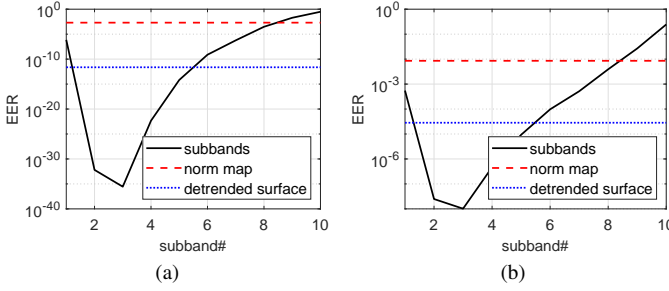


Fig. 11. EER calculated for every subband when correlation values are believed to follow (a) Gaussian or (b) Laplace distributions. The reference data is obtained by a confocal microscope and the test data is acquired with flatbed scanners. The third-highest spatial-frequency subband is the most powerful in describing the uniqueness of physical surfaces. Horizontal lines correspond to the performance when the norm map or detrended surface/heightmap is used as the discriminative feature.

using flatbed scanners acquired images. We follow the procedure in [11] to reconstruct 3D heightmaps of paper patches and derive the subbands of the reconstructed heightmaps for authentication. The reference data is from confocal microscope, each paper patch was scanned once by the confocal microscope. The test data is obtained from scanners. Each paper patch was scanned by one scanner three times, and there are three different scanners used. Thus, each paper patch has one ground-truth heightmap from confocal microscope and nine reconstructed heightmaps from scanners.

Here, we summarize the benefit of using detrended heightmaps and more details are given in Section A of the supplementary document. The correlation value using reconstructed heightmaps improved to 0.358 from 0.357 or 0.301 when using the norm map as the discriminative feature, as shown in Table I. When using the detrended heightmap as discriminative feature, the correlation value further improved to 0.499. This result is consistent with that reported in [11] where mobile camera was used as the acquisitions device. Hence, the detrended heightmap is a more powerful discriminative feature than the norm map.

We also summarize the benefit of using high spatial-frequency subbands of heightmaps and more details are given in Section B of the supplementary document. We decomposed the reconstructed heightmap into ten spatial subbands corresponding to a DoG representation as reviewed in Section II-A. Using the third-highest spatial-frequency subband instead of the detrended heightmap, the correlation value improved from 0.499 to 0.714. The estimated EER as a function of subband index is shown in Fig. 11, and a smaller subband index corresponds to a higher spatial frequency. When using the third-highest spatial-frequency subband, the EER achieved 10^{-36} or 10^{-8} under the Gaussian or Laplacian tail extrapolation assumption, which is a large improvement than 10^{-11} or $10^{-4.5}$ when using detrended heightmap. The high spatial-frequency subbands are more powerful discriminative features than detrended heightmaps when using flatbed scanners for paper surface-based authentication.

C. Practical Authentication System

In this subsection, we examine a practical authentication system that uses flatbed scanners to acquire both test and reference data. We compare using every subband of heightmap as the discriminative feature to the traditional feature, i.e., the norm map, and measure the authentication performance in EER. The diagrams for generating the subbands in the authentication system for test and reference patches are shown in Figs. 10(a) and (c), respectively. The reference and test patches are both images acquired by scanners.

In the practical authentication system, we use scanners to capture the reference data instead of using the confocal microscope because scanners are easier to automate and more affordable for practical deployment. Each paper patch was scanned three times by each of the three scanners. We obtained nine norm maps using scanners for each paper patch. For the matched case, we chose two norm maps from the nine norm maps each time as a test-reference pair, forming a total of 36 pairs for each paper patch. Given the nine physical pieces of paper patches, this leads to a total of $36 \times 9 = 324$ data points of correlation values for statistical analysis. For the unmatched case, each paper patch pair gives $9 \times 9 = 81$ data points, and there are $\binom{9}{2} = 36$ paper patch pairs. Theoretically there are totally $81 \times 36 = 2916$ data points if using all paper patches. To mimic a practical scenario, we randomly chose one paper patch from the rest paper patches to obtain the reference data, leading to a random subset of 729 data points for the unmatched case.

We reconstructed 3D surfaces from the norm maps and obtained the subbands of the heightmap as the discriminative features. We calculated the correlation values of subbands between the test and reference data. We calculated the EER for every subband and plotted the results in Fig. 12. When correlation values are believed to follow Gaussian or Laplace distributions, the EER are about 10^{-157} and 10^{-17} at the second-highest spatial-frequency subband, respectively. We also compared the performance of subbands of heightmap to that of the norm map and detrended heightmap, as shown by horizontal lines in Fig. 12 and they are much larger than using the second-highest spatial-frequency subband. Hence, in the practical system that uses scanner to acquire reference data, the authentication performance of the second-highest spatial-frequency subband is much better than that of the norm map or detrended surfaces in terms of EER. In Table II, we summarized the authentication performance of the practical authentication system in this work. For comparison, we also reproduced the results in [11] where mobile cameras instead of scanners were used to obtain the test data. We compared the best EER of the subbands when assuming the correlation values are Gaussian and Laplacian distributed. The performance of the practical authentication system in this work using scanners to obtain test data is much better than using mobile camera in terms of EER.

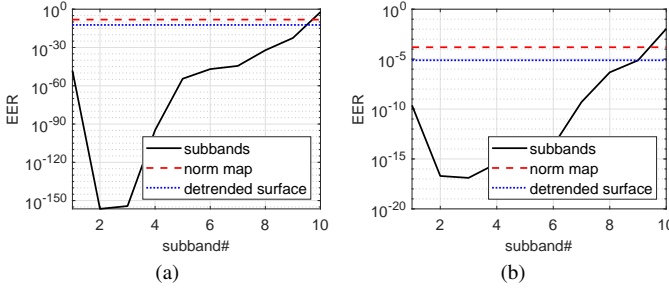


Fig. 12. EER calculated for every subband when correlation values are believed to follow (a) Gaussian or (b) Laplace distributions. The second-highest spatial-frequency subband has the most powerful authentication capability in a practical setup that scanners are used to acquire reference data. Horizontal lines correspond to the performance when the norm map or detrended surface/heightmap is used as the discriminative feature.

TABLE II
COMPARISON OF PERFORMANCE OF PRACTICAL AUTHENTICATION SYSTEM WHEN TEST DATA IS OBTAINED FROM MOBILE CAMERA OR SCANNER

Test device	Reference device	Feature	EER (Gaussian and Laplacian)
mobile camera	scanner	norm map	10^{-5} and 10^{-3} [11]
mobile camera	scanner	subband	10^{-8} and 10^{-3} [11]
scanner	scanner	norm map	10^{-9} and 10^{-4}
scanner	scanner	subband	10^{-157} and 10^{-17}

VI. SIZE OF PAPER PATCH, DIGITIZATION RESOLUTION, AND PERTURBATION OF ALIGNMENT

A. How Large Should the Size of Paper Patch Be?

Throughout the experiments of this work, the size of paper patch was fixed to be $\frac{2}{3}$ -by- $\frac{2}{3}$ inch² and discretized to 200-by-200 pixels. A natural research question pertaining to a practical deployment is: How does the size of paper patch affect the authentication performance? To investigate this question, we successively cut one heightmap into four heightmaps, empirically calculated the EER using the smaller heightmaps after each cut, and examined how EER change as the number of cuts increases. More specifically, we regarded the heightmap's center 160-by-160 pixels as the root patch that had not been cut. After the first cut, the resulting heightmaps were of the size 80-by-80 pixels. At each cut level, we calculated the correlation values against confocal references. We observed that, after each cut, the mean of correlation values were almost unchanged, whereas the standard deviation would increase by a factor of ~ 2 times for unmatched cases and ~ 1.5 times for matches cases. We plotted the sample standard deviations of the correlation values as a function of the number of cuts in Fig. 13. We further calculated EERs at each cutting level and plotted EERs against the block edge size in Fig. 14, in which block edge size = 1 corresponds to using 160 pixels. As expected, the authentication performance in EER improves as the block size increases.

Below, we analytically show that the EER is exponentially decreasing in the size of paper patch when correlation values are assumed to be Laplacian distributed. Using (21b) and the variance formula of a Laplace random variable, $\lambda = \sqrt{2}/\sigma$,

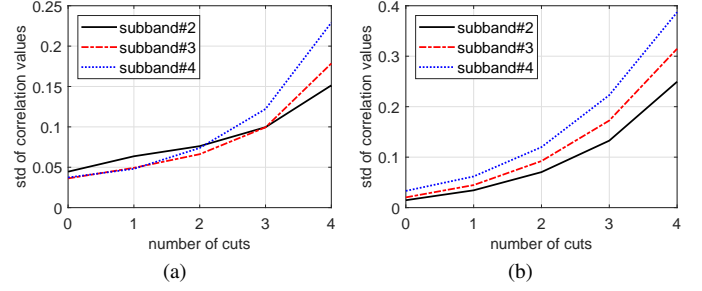


Fig. 13. Sample standard deviations of the correlation values when cutting paper patch into blocks under (a) matched and (b) unmatched cases. The standard deviations of the correlation values in spatial-frequency subbands #2-#4 increase exponentially when cutting paper patch into small blocks.

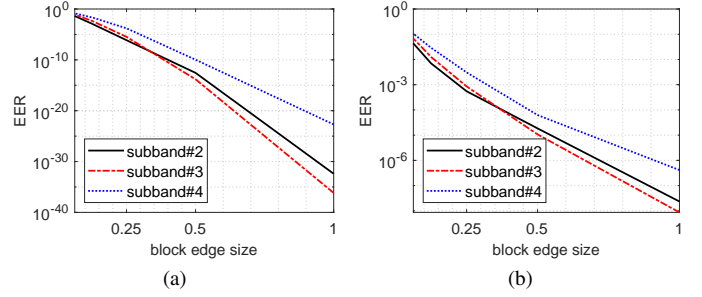


Fig. 14. After cutting paper patch into blocks, EERs against the block edge length when assuming (a) Gaussian and (b) Laplace distributions. Size of 1 corresponds to the edge length of the original patch. The EERs decrease when the block edge length increases.

the EER can be rewritten as $\text{EER} = \frac{1}{2} \exp \left[\frac{\sqrt{2}}{\sigma_0 + \sigma_1} (\mu_0 - \mu_1) \right]$. After n cuts, EER can be expressed as

$$\text{EER}(n) = \frac{1}{2} \exp \left[\frac{\sqrt{2}}{2^n \sigma_0 + 1.5^n \sigma_1} (\mu_0 - \mu_1) \right] \quad (13a)$$

$$\approx \frac{1}{2} \exp \left[\sqrt{2} \cdot 2^{-n} (\mu_0 - \mu_1) / \sigma_0 \right], \quad (13b)$$

where (13a) incorporates the empirically observed exponential increase of the standard deviations in the previous paragraph, and (13b) is approximately true for large n . Since 2^{-n} is proportional to the block edge size after n cuts, $\log(\text{EER}(n))$ is linearly decreasing in the block edge length, which is consistent with Fig. 14(b). When the edge length decreases from 160 pixels (or 0.53 inch) to 80 pixels (or 0.27 inch), the performance drops from around 10^{-9} to 10^{-5} in EER. To conclude, larger patch size will lead to better authentication performance, and given a certain paper type, experiments similar to the one demonstrated in this subsection may be conducted to determine the patch size needed to achieve a certain performance level.

Below, we justify the exponential increase of the standard deviation for correlation values as the number of cuts increases. First, we claim the following finite-sample relation between the sample correlation coefficient of a block, ρ , and the sample correlation coefficients of its nonoverlapping, equal-sized subblocks, $\{\rho_i\}_{i=1}^4$, namely,

$$\rho \approx \frac{1}{4} \sum_{i=1}^4 \rho_i. \quad (14)$$

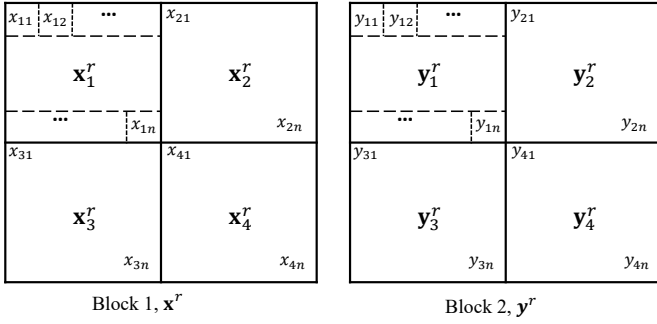


Fig. 15. Sample correlation coefficients: ρ , between two blocks; ρ_i , between two collocated subblocks with index i . Detailed definitions are as follows: $\rho_i = \text{Corr}(\mathbf{x}_i^r, \mathbf{y}_i^r)$, $i = 1, \dots, 4$, and $\rho = \text{Corr}(\mathbf{x}^r, \mathbf{y}^r)$, where the superscript “ r ” stands for the raw image data before sample mean is removed. \mathbf{x}_i^r and \mathbf{y}_i^r are length- n column vectors containing all pixel values of the respective subblocks. \mathbf{x}^r and \mathbf{y}^r are concatenated column vectors where $\mathbf{x}^r = (\mathbf{x}_1^r, \dots, \mathbf{x}_4^r)$ and $\mathbf{y}^r = (\mathbf{y}_1^r, \dots, \mathbf{y}_4^r)$.

The blocks and subblocks are illustrated in Fig. 15, and ρ and ρ_i 's are defined in the caption. The relation of (14) is justified in the Appendix with a proof in the asymptotic case and an observation in the finite-sample case. With the claimed relationship (14), we investigate the increase in variance after one cut. We consider the correlation values $\{\rho_i\}_{i=1}^4$ as random variables that are identically distributed. In the unmatched scenario, the correlation values should have a zero mean and correlation values produced by neighboring blocks that do not have reasons to be dependent. We used experimental results to confirm that $\text{Cov}(\rho_i, \rho_{i'}) = 0, \forall i \neq i'$, for the unmatched case. After cutting the heightmap into four subblocks, we calculated correlation values $\{\rho_i\}_{i=1}^4$. There were 81 correlation values for the i th block location, and we ordered them into a vector ρ_i . We used the sample correlation value $\text{Corr}(\rho_i, \rho_{i'})$ to estimate the theoretical quantity $\text{Corr}(\rho_i, \rho_{i'})$. The sample mean and standard deviation values of correlation values $\text{Corr}(\rho_i, \rho_{i'})$ for subbands #2–#4 are around -0.1 and 0.2 , respectively. A t -test shows that the correlation values are not significantly different from zero (p -value = 0.249), which supports our hypothesis. Hence, by applying the variance operation to (14) and using $\text{Cov}(\rho_i, \rho_{i'}) = 0$, we obtain for the unmatched scenario:

$$\text{Var}(\rho_1) = 4 \text{Var}(\rho). \quad (15)$$

Therefore, after one cut the standard deviation of the correlation values will increase by a factor of 2, which is consistent with the aforementioned empirical observation. For the matched case, the correlation values produced by neighboring blocks should be positively correlated, i.e., $\text{Cov}(\rho_i, \rho_{i'}) > 0$ for $i \neq i'$. For example, $\{\rho_i\}_{i=1}^4$ are likely to be simultaneously all high or all low, but it is less likely to have two high values and two low values. We calculated the sample correlation value $\text{Corr}(\rho_i, \rho_{i'})$. The sample mean and standard deviation values of correlation values $\text{Corr}(\rho_i, \rho_{i'})$ for subbands #2–#4 are around 0.4 and 0.2 . A t -test shows that the correlation values are significantly larger than zero (p -value = 8.48×10^{-8}), which also supports our hypothesis. Applying the variance operation to (14) and considering the

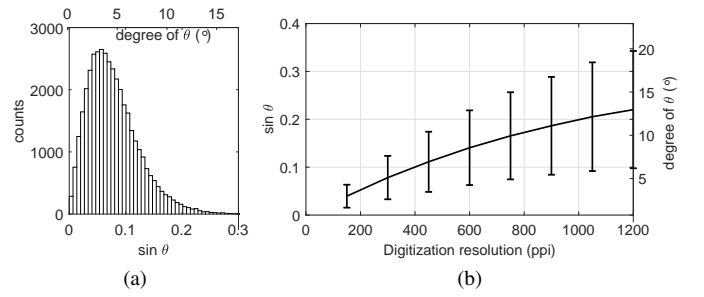


Fig. 16. (a) Histogram of the orientation of squared area covered by a working pixel when a paper patch of size $\frac{2}{3}$ -by- $\frac{2}{3}$ inch² is digitized to 200-by-200 working pixels or 300 ppi. (b) The averaged orientation as a function of digitization resolution. Error bars correspond to one sample standard deviation above and below the average. The monotonic smoothly increasing curve does not strongly justify the use of a particular resolution among others within the interior of $[150, 1200]$ ppi.

positive correlation among ρ_i 's, we obtain for the matched scenario:

$$\text{Var}(\rho_1) = 4 \text{Var}(\rho) - \frac{1}{2} \sum_{i \neq i'} \text{Cov}(\rho_i, \rho_{i'}) < 4 \text{Var}(\rho), \quad (16)$$

which corresponds to an increase in standard deviation by a factor of less than 2 after one cut, which is also consistent with the empirical observation of a factor of 1.5.

B. Resolution of Norm Map

Another research question closely related to the issue of the patch size studied in the previous subsection is the choice of resolution for digitizing the patch. The resolution used in the experiments of this work is 300 pixels per inch (ppi) or 84.7 μm per pixel, i.e., a patch of $\frac{2}{3}$ -by- $\frac{2}{3}$ inch² is digitized to 200-by-200 working pixels. According to Section VII.C and Fig. 14 of [10], within the squared regions of the size of a working pixel, most surfaces “were not flat because the scale of fibers is smaller than the area of a working pixel.” Shall we reduce the size of working pixels so that the surfaces correspond to pixels can be more flat so as to improve the characterization of the structure of the paper, and in turn, improve the authentication performance?

We first examine the distribution of the orientations of squared areas of the size of a working pixel when a paper patch of size $\frac{2}{3}$ -by- $\frac{2}{3}$ inch² is digitized to 300 ppi. We use the tangent plane algorithm in [10] to obtain surface normal vectors using a heightmap captured by a confocal microscope. We denote the angle formed by the surface normal vector and z -axis by θ . A histogram for the sine of working pixel's orientation, $\sin \theta$, is shown in Fig. 16(a), with a sample mean of 0.078 (or 4.5°) and sample standard deviation of 0.045 (or 2.6°) for $\sin \theta$. These estimated angles are very small compared to the actual angles that could be formed by intertwined fibers. However, when considering a relatively larger area covered by a working pixel that may contain multiple fibers segments, it is reasonable that prominently tilted structures are smoothed out.

Next, we increase the resolution of the norm map to see how the distribution of surface orientation may change, and whether there exists any resolution that outperforms others.

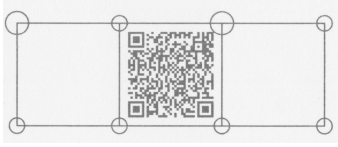


Fig. 17. The design of a registration pattern used in this work. The image was captured by a flatbed scanner. The square patch on the left of the QR code is the area used by authentication. By detecting the QR code, the location of the pattern in the image can be roughly estimated, then the precise location is estimated using the lines and circles. Also, the QR code can be used to store information such as paper ID and the reference feature.

We vary the resolution ranges from 150 to 1200 ppi to cover a practical working range for consumer-grade flatbed scanners. As we increase the resolution, working pixels will shrink in size, leading to larger estimated angles. At each resolution level, we calculate the sample mean and sample standard deviation of $\sin \theta$ and plot the results in Fig. 16(b). The plot reveals that both average angle and the angle variation increase as the resolution increases, which is reasonable since finer details of the microstructure of paper surface are captured. This means that using higher resolution (and a fixed number of pixels), a digitized normal vector field is likely to contain more randomness and therefore can potentially lead to higher authentication performance by reducing the false negative rate. However, this monotonic smoothly increasing curve does not strongly justify the use of a particular resolution among others within the interior of the interval ranges from 150 to 1200 ppi. In our proof-of-concept work, we stick to the current digitization resolution, i.e., 300 ppi, so that the resolution is adequate for authentication while keeping the computationally complexity at a reasonable level.

C. Impact of Spatial Registration Error

In this subsection, we investigate the performance drop due to the error of spatial registration for the paper patch. Clarkson et al. [4] applied a lowpass filter to the extracted image and downsampled it to reduce the impact of the registration error, but its effect was not explicitly studied. Fig. 17 shows an image of a piece of paper scanned by a flatbed scanner, which shows the design of a registration pattern we used in this work. The square patch to the left of the QR code patch is the area of interest that we use for paper surface-based authentication. To locate the position of the area of interest, we need to estimate the positions of the intersections. We first use Hough transform to find the lines and then the intersections. We then refine the estimations for the positions of intersections by finding the centers of the circles. The intersections of the lines in the paper patch are printed in the center of respective circles.

In the real-world application, the estimations for the positions of the paper patch may be inaccurate, and as a result, the performance will drop. To investigate the effect of imprecise estimations for the positions, we perturbate the estimated locations of the four corner positions of the paper patch. For each of the estimated corner location (x, y) , we add some noise to it, namely, $x' = x + e_1$, $y' = y + e_2$, where $e_1, e_2 \sim \mathcal{N}(0, L^2)$, L is standard deviation to indicate the level of perturbation strength. We follow the procedure in the

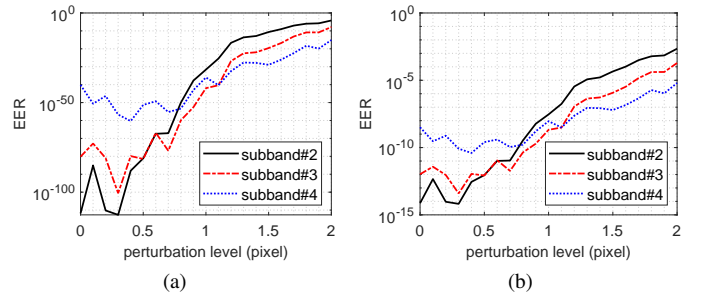


Fig. 18. The impact of spatial registration error: EERs against the perturbation strength L when assuming (a) Gaussian and (b) Laplace distributions. The length of a pixel edge is $\frac{1}{300}$ inches. When there is more registration error (or larger perturbation), the discriminative performance is significantly lowered.

practical authentication system in Section V-C while adding perturbations to the estimated corner positions in each scanned image of the paper patch. We increase the perturbation strength L and calculate the EER at each perturbation strength level, and plot the results in Fig. 18. When the perturbation strength is small, within 0.3 pixels, the EERs does not change much. This may be due to the fact that the estimated corner positions of the paper patch were not very accurate in the first place, thus adding small perturbations did not result in much performance drop. As the perturbation strength increased beyond 0.4 pixels, the EERs will increase significantly, indicating that deploying a precise image alignment algorithm is one important factor to achieving satisfactory authentication performance.

VII. CONCLUSION

In this paper, we have investigated the paper surface-based authentication using the flatbed scanners. We have shown by analytic derivations that the specular component of light reflection does not play a role in the estimation of the norm map of paper surfaces in the unique optical setup of a flatbed scanner. We used a larger dataset to confirm that flatbed scanners can capture meaningful physical quantities of paper surfaces and investigated the blurring effect due to the scanner. We have shown that the high frequency subbands of the reconstructed surfaces are better discriminative features than the norm map and verified it in a practical engineering system that uses flatbed scanners. We have shown that larger paper patches will yield better authentication performance in EER and precise image alignment algorithm is important for achieving satisfactory authentication performance. In future work, we plan to investigate key research questions on using mobile cameras to acquire the microstructure, e.g., how the specular reflection can be taken into consideration to improve the estimation accuracy of the norm map.

APPENDIX

JUSTIFICATION FOR $\rho \approx 1/4 \sum_{i=1}^4 \rho_i$

We will provide justification for the relation (14) between the sample correlation coefficient of a block, ρ , and the sample correlation coefficients of its nonoverlapping, equal-sized subblocks, $\{\rho_i\}_{i=1}^4$, namely, $\rho \approx 1/4 \sum_{i=1}^4 \rho_i$. We will argue in the finite-sample case that the residual $r_n =$

$\rho - \frac{1}{4} \sum_{i=1}^4 \rho_i \approx 0$. We will also prove that in the asymptotic case $|r_n|$ converges to 0 in probability.

We denote, for i th subblock, the raw data $\mathbf{x}_i^r = (x_{i1}, x_{i2}, \dots, x_{in})$, the sample mean $x_{i\cdot} = \frac{1}{n} \sum_{j=1}^n x_{ij}$, and the mean-removed data $\mathbf{x}_i = \mathbf{x}_i^r - x_{i\cdot}$, where $i \in \{1, 2, 3, 4\}$. The mean-removed data for the parent block can be represented as follows:

$$\mathbf{x} \stackrel{(a)}{=} \begin{bmatrix} \mathbf{x}_1^r \\ \vdots \\ \mathbf{x}_4^r \end{bmatrix} - \frac{1}{4} \sum_{i=1}^4 x_{i\cdot} \stackrel{(b)}{=} \begin{bmatrix} \mathbf{x}_1 \\ \vdots \\ \mathbf{x}_4 \end{bmatrix} + \begin{bmatrix} \epsilon_1 \mathbb{1} \\ \vdots \\ \epsilon_4 \mathbb{1} \end{bmatrix} \stackrel{(c)}{=} \mathbf{x}' + \epsilon, \quad (17)$$

where $\mathbb{1}$ is length- n vector of all ones, and $\epsilon_i = \frac{1}{4}(3x_{i\cdot} - \sum_{i' \neq i} x_{i'\cdot})$ is a perturbation term. Here, (17a) and (17c) is by definition. (17b) connects the mean-removed terms \mathbf{x} and $\{\mathbf{x}_i\}_{i=1}^4$ at two scales. With the definitions of \mathbf{x} and $\{\mathbf{x}_i\}_{i=1}^4$, ρ and ρ_i defined in the caption of Fig. 15 can be rewritten as:

$$\rho = \frac{\mathbf{x}^T \mathbf{y}}{\|\mathbf{x}\| \|\mathbf{y}\|}, \quad \rho_i = \frac{\mathbf{x}_i^T \mathbf{y}_i}{\|\mathbf{x}_i\| \|\mathbf{y}_i\|}, \quad i = 1, \dots, 4. \quad (18)$$

Finite-sample approximation For a finite sample size, we justify the following relationship by showing perturbation terms are close to zero and $\|\mathbf{x}_i\|$ s are close to $\|\mathbf{x}\|/2$:

$$r_n = \sum_{i=1}^4 \mathbf{x}_i^T \mathbf{y}_i \left(\frac{1}{\|\mathbf{x}\| \|\mathbf{y}\|} - \frac{1}{4 \|\mathbf{x}_i\| \|\mathbf{y}_i\|} \right) + [\mathbb{1}^T (\epsilon_i \mathbf{x}_i + \varepsilon_i \mathbf{y}_i) + n \epsilon_i \varepsilon_i] / \|\mathbf{x}\| \|\mathbf{y}\| \approx 0. \quad (19)$$

Assume that x_{ij} 's are independent and identically distributed with mean value μ and variance σ^2 . Note that $\|\mathbf{x}_i\|^2 = \sum_{j=1}^n x_{ij}^2 - n x_{i\cdot}^2$. It is easy to show using the strong law of large number that $\|\mathbf{x}_i\|^2$ converges to $n\sigma^2$ almost surely, and $\|\mathbf{x}\|^2$ converges to $4n\sigma^2$ almost surely. Hence, the term in the parentheses of (19) is close to zero. Both perturbation terms ϵ_i and $\varepsilon_i \sim \mathcal{N}(0, 0.75\sigma^2/n)$ are zero mean with very tiny variance for large n , e.g., $n = 10000$ in our application scenario. Hence, the term in the brackets is also close to zero. We also used real data to verify that $r_n \approx 0$. We followed the procedures in Section VI-A to cut the subbands into four subblocks and calculate the sample correlation values ρ and ρ_i , $i = 1, \dots, 4$. Under the matched case, i.e., the population correlation is larger than zero, the sample mean and standard deviation of r_n for subbands #2–#4 were around 10^{-5} and 10^{-3} , respectively. Under the unmatched case, i.e., the population correlation is zero, the sample mean and standard deviation of r_n for subbands #2–#4 were around 10^{-4} and 10^{-3} , respectively. The small residuals confirmed that $r_n \approx 0$ for the finite-sample scenario.

Lemma 1. [23] When population correlation value ρ_t of a bivariate Gaussian pair is nonzero, the expectation and variance of sample correlation value ρ can be expressed in the form of series: $\mathbb{E}[\rho] = \rho_t - \frac{\rho_t(1-\rho_t^2)}{2(n-1)} + \dots$, $\text{Var}(\rho) = \frac{(1-\rho_t^2)^2}{n-1} \left[1 + \frac{11\rho_t^2}{2(4n-1)} + \dots \right]$, where n is the sample size.

Convergence in mean Denote the population correlation value to be ρ_t . The sample size is $4n$ for the block and n for a subblock. From Lemma 1, we have: $\mathbb{E} \left[\rho - \frac{1}{4} \sum_{i=1}^4 \rho_i \right] =$

$$\left(\rho_t - \frac{\rho_t(1-\rho_t^2)}{2(4n-1)} + \dots \right) - \frac{1}{4} \sum_{i=1}^4 \left(\rho_t - \frac{\rho_t(1-\rho_t^2)}{2(n-1)} + \dots \right) \rightarrow 0 \text{ as } n \rightarrow \infty.$$

Convergence in probability For a sample correlation ρ in a block, from Lemma 1 and Markov's inequality we can derive:

$$\mathbb{P}(|\rho - \rho_t| > \varepsilon) \leq (\text{Var}(\rho) + (\mathbb{E}(\rho) - \rho_t)^2) / \varepsilon^2 = 1/\varepsilon^2 \cdot \left[\frac{(1-\rho_t^2)^2}{4n-1} \left(1 + \frac{11\rho_t^2}{2(4n-1)} + \dots \right) + \left(\frac{\rho_t(1-\rho_t^2)}{2(4n-1)} + \dots \right)^2 \right], \quad (20)$$

which is easy to show that $\mathbb{P}[|\rho - \rho_t| > \varepsilon] \rightarrow 0$ and hence ρ converges to ρ_t in probability, or in a slightly different form $|\rho - \rho_t| \xrightarrow{p} 0$. Similarly, $|\rho_i - \rho_t| \xrightarrow{p} 0$. From triangle inequality, we have $|\rho_i - \rho| \leq |\rho_i - \rho_t| + |\rho_t - \rho| \xrightarrow{p} 0$. Applying triangle inequality again, we conclude the proof: $|r_n| = \frac{1}{4} \left| \sum_{i=1}^4 (\rho_i - \rho) \right| \leq \frac{1}{4} \sum_{i=1}^4 |\rho_i - \rho| \xrightarrow{p} 0$.

REFERENCES

- [1] "The paper project," Retrieved Feb. 2019. [Online]. Available: <http://www.paperproject.org/>
- [2] Y. D. Kariakin, "Authentication of articles," Oct. 7 1997, patent WO9724699A1.
- [3] J. D. Buchanan, R. P. Cowburn, A.-V. Jausovec, D. Petit, P. Seem, G. Xiong, D. Atkinson, K. Fenton, D. A. Allwood, and M. T. Bryan, "Forgery: 'Fingerprinting' documents and packaging," *Nature*, vol. 436, no. 7050, p. 475, 2005.
- [4] W. Clarkson, T. Weyrich, A. Finkelstein, N. Heninger, J. Halderman, and E. Felten, "Fingerprinting blank paper using commodity scanners," in *IEEE Symposium on Security and Privacy*, Berkeley, CA, May 2009, pp. 301–314.
- [5] S. Voloshynovskiy, M. Diephuis, F. Beekhof, O. Koval, and B. Keel, "Towards reproducible results in authentication based on physical non-cloneable functions: The forensic authentication microstructure optical set (FAMOS)," in *IEEE International Workshop on Information Forensics and Security*, Tenerife, Spain, Dec. 2012, pp. 43–48.
- [6] M. Diephuis and S. Voloshynovskiy, "Physical object identification based on FAMOS microstructure fingerprinting: Comparison of templates versus invariant features," in *International Symposium on Image and Signal Processing and Analysis*, Trieste, Italy, Sep. 2013, pp. 119–123.
- [7] M. Diephuis, S. Voloshynovskiy, T. Holtyak, N. Stendardo, and B. Keel, "A framework for fast and secure packaging identification on mobile phones," in *Proc. SPIE, Media Watermarking, Security, and Forensics*, San Francisco, CA, Feb. 2014, p. 90280T.
- [8] C.-W. Wong and M. Wu, "A study on PUF characteristics for counterfeiting detection," in *IEEE International Conference on Image Processing*, Quebec City, Canada, Sep. 2015, pp. 1643–1647.
- [9] —, "Counterfeit detection using paper PUF and mobile cameras," in *IEEE International Workshop on Information Forensics and Security*, Rome, Italy, Nov. 2015.
- [10] —, "Counterfeit detection based on unclonable feature of paper using mobile camera," *IEEE Transactions on Information Forensics and Security*, vol. 12, no. 8, pp. 1885–1899, Apr. 2017.
- [11] R. Liu, C.-W. Wong, and M. Wu, "Enhanced geometric reflection models for paper surface based authentication," in *IEEE International Workshop on Information Forensics and Security*, Hong Kong, Dec. 2018.
- [12] C. Kauba, L. Debiasi, R. Schraml, and A. Uhl, "Towards drug counterfeit detection using package paperboard classification," in *Pacific Rim Conference on Multimedia*. Springer, 2016, pp. 136–146.
- [13] R. Schraml, L. Debiasi, C. Kauba, and A. Uhl, "On the feasibility of classification-based product package authentication," in *IEEE Workshop on Information Forensics and Security*, 2017.
- [14] F. Beekhof, S. Voloshynovskiy, O. Koval, R. Villán, and T. Pun, "Secure surface identification codes," in *Security, Forensics, Steganography, and Watermarking of Multimedia Contents X*, vol. 6819. International Society for Optics and Photonics, 2008, p. 68190D.
- [15] A. Sharma, L. Subramanian, and E. A. Brewer, "Paperspeckle: Microscopic fingerprinting of paper," in *ACM Conference on Computer and Communications Security*. ACM, 2011, pp. 99–110.
- [16] E. Toreini, S. F. Shahandashti, and F. Hao, "Texture to the rescue: Practical paper fingerprinting based on texture patterns," *ACM Transactions on Privacy and Security (TOPS)*, vol. 20, no. 3, p. 9, 2017.

- [17] R. Szeliski, *Computer Vision: Algorithms and Applications*. Springer, 2010, ch. 2.2.
- [18] R. Hartley and A. Zisserman, *Multiple view geometry in computer vision*. Cambridge University Press, 2003.
- [19] D. G. Lowe, "Distinctive image features from scale-invariant keypoints," *International Journal of Computer Vision*, vol. 60, no. 2, pp. 91–110, 2004.
- [20] T. Lindeberg, "Scale-space theory: A basic tool for analyzing structures at different scales," *Journal of Applied Statistics*, vol. 21, no. 1-2, pp. 225–270, 1994.
- [21] P. Kovsi, "Shapelets correlated with surface normals produce surfaces," in *IEEE International Conference on Computer Vision*, Beijing, China, Oct. 2005, pp. 994–1001.
- [22] M.-C. Beland and J. M. Bennett, "Effect of local microroughness on the gloss uniformity of printed paper surfaces," *Applied Optics*, vol. 39, no. 16, pp. 2719–2726, Jun. 2000.
- [23] J. F. Kenney and E. Keeping, *Mathematics of Statistics, Vol. II*. New York: D. Van Nostrand Co. Inc, 1951.
- [24] J. L. Devore, *Probability and Statistics for Engineering and the Sciences*. Cengage Learning, 2011.

SUPPLEMENTARY DOCUMENT

A. Reconstructed Heightmap Leads to Higher Correlation

We follow [11] to reconstruct heightmaps with normal vector fields generated from scanners and confocal using shapelet [21] that can be considered as a robust integration algorithm. The diagrams for generating the heightmaps/3D surfaces for test and reference patches are shown in Figs. 10(a) and (b), respectively, excluding the last blocks. The images for the test patch are acquired by scanners and the heightmap for the reference patch is measured by confocal microscope. We correlated the reconstructed heightmaps between scanner and confocal, obtaining the correlation at 0.358 as shown in Table I, which is higher than the correlation at 0.357 or 0.301 using the norm map as the feature. The improved correlation values indicate that the heightmap with integrated information in both x - and y -directions is a better discriminative feature than the norm map.

Fig. 19(a) shows a reconstructed heightmap from images acquired by a scanner. It is observed that the right part of the paper patch has a higher elevation than the left part. This may be caused by the nonflat shape of the paper when being scanned that is not a stable characteristic and may change every time the paper is handled. The global trend due to the nonflat shape is also problematic from the perspective of the similarity measure using correlation coefficient: i) if two surfaces have similar trends, the correlation between the two surfaces will be high even if their local structures are very different; ii) if trends are different, correlation will be low even if their local structures similar. Hence, the trend of heightmaps must be removed before correlation is calculated.

We removed the trend of the heightmap in Fig. 19(a) and a detrended version is shown in Fig. 19(b). The detrending process contains two steps. First, a Gaussian blur was applied to generate a surface capturing the overall trend of the heightmap but not capturing the local structures. In the experiments of this paper in which $\frac{2}{3}$ -by- $\frac{2}{3}$ inch² patches are digitized to 200-by-200 pixels, a standard deviation of 25 pixels was a reasonable value. Second, the trend surface was subtracted from the heightmap to generate the detrended heightmap.

The correlation resulted from using the detrended heightmap is 0.499, which is a further improvement over 0.358 resulted from using the raw heightmap. This result is consistent with that reported in [11] that studied cameras as acquisition device. Note that the detrended surface retains the middle to high spatial-frequency contents of the raw heightmap that corresponds to local structures, since the trend surface containing the low frequency contents was removed.

B. Discrimination Using Subbands of Heightmap

The diagrams for generating the subbands of heightmaps/3D surfaces for test and reference patches are shown in Figs. 10(a) and (b), respectively, including the last blocks. We decompose the reconstructed heightmap into ten spatial subbands corresponding to a DoG representation. We plot representative slices of the original heightmap in Fig. 20(a) and the third-highest subband, i.e., SUBBAND#3 in Fig. 20(b).

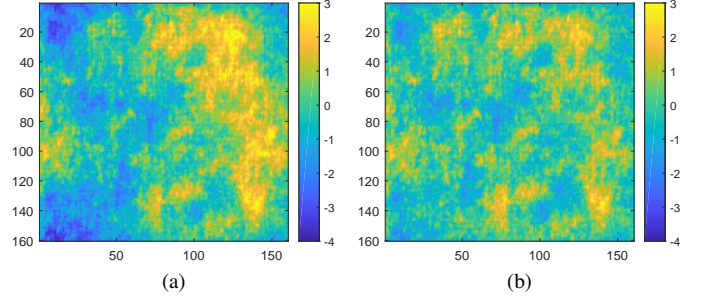


Fig. 19. (a) Reconstructed heightmap from a norm map estimated from images acquired by a scanner, and (b) a detrended version of (a). The detrended heightmap is more flat and local peaks and valleys are more visible.

Fig. 20(a) reveals the trends in the reconstructed surface from scanners. Fig. 20(b) shows that the high-spatial frequency subbands from scanner and confocal microscope match well with each other. We calculated the correlation when scanner matches (H_0) or does not match (H_1) the confocal for every subband. The distributions of correlation values for each subband is shown in Fig. 21. The distances of distributions for matched and unmatched in high spatial-frequency subbands are far, indicating a good discriminative capability. The averaged correlation for best performing subband, i.e., the third-highest spatial-frequency subband, is 0.714 as shown in Table I.

We quantitatively evaluate the discriminative performance of each spatial subband of the heightmap. For the majority of them, i.e., Subbands #1 to #8, the empirical distributions for two hypotheses do not have overlap as shown in Fig. 21. This also poses a difficulty in estimating discrimination quantities such as the probability of false alarm or miss when the threshold used is in the middle of two distributions. This issue is caused by the fact that the overlapping tails are too tiny. We follow the procedure laid out in [10] to obtain the maximum likelihood estimator (MLE) of the EER using summary statistic quantities of each hypothesis. Since EER is achieved when both false-alarm and miss rates are small and equal, the characteristics of extrapolated tails affect the final result significantly. Since there are not enough data for determining the behaviors of the tails, we use a light-tailed distribution, Gaussian, and a heavy-tailed distribution, Laplacian, to quantify the ERR in an optimistic way and a pessimistic way, respectively. It is not difficult to show that when correlation is assumed to be Gaussian and Laplacian and using a simple thresholding rule, EER can be written as

$$\text{EER} = \Phi[(\mu_0 - \mu_1)/(\sigma_0 + \sigma_1)], \quad (21a)$$

$$\text{EER} = \frac{1}{2} \exp[(\mu_0 - \mu_1) \cdot \lambda_0 \lambda_1 / (\lambda_0 + \lambda_1)], \quad (21b)$$

respectively, where $\Phi(\cdot)$ is cumulative density function for the standard Gaussian distribution, and μ_i and σ_i , $i = 0, 1$ are mean and standard deviation for the i th hypothesis. By the invariance principle [24], we could substitute MLE estimates for μ_i and σ_i into the above equations to obtain the MLE for EER.

The estimated EER as a function of subband index is shown in Fig. 11. It is revealed that the third-highest spatial-frequency

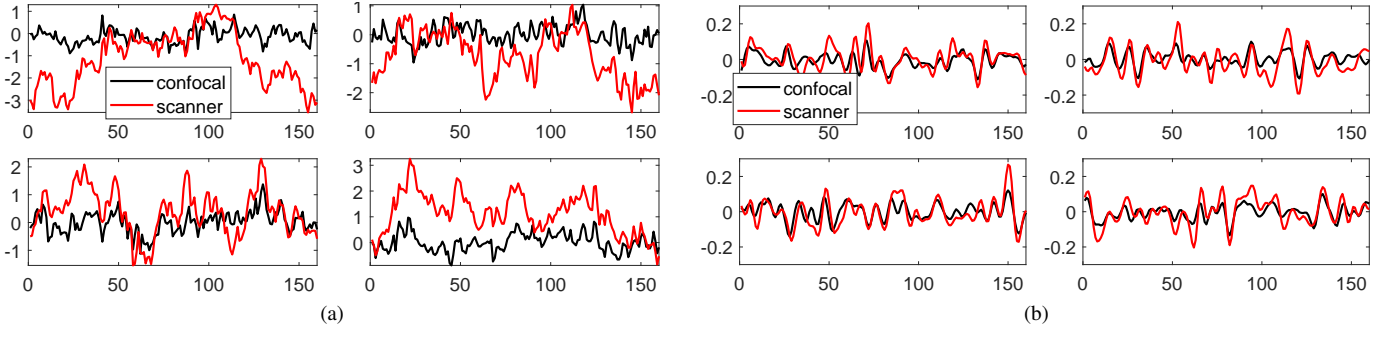


Fig. 20. Representative slices in x direction from (a) original heightmap and (b) SUBBAND#3. The slices in the heightmaps of scanner have trends. The peaks in the high-spatial frequency subbands overlap much better than in the original heightmaps.

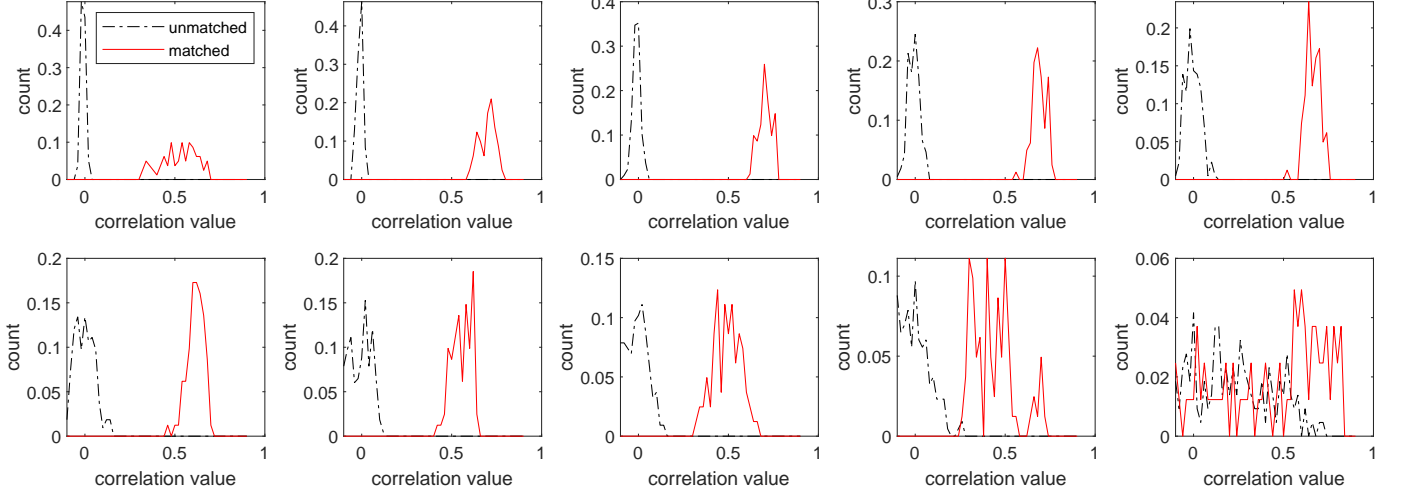


Fig. 21. Distributions of correlation values for matched cases and unmatched cases at different subbands. The second and third-highest spatial-frequency subbands are more powerful in describing the uniqueness of physical surfaces.

subband is the most discriminative, achieving an ERR at 10^{-36} or 10^{-8} under the Gaussian or Laplacian tail extrapolation assumption. We also compare the performance of subbands of heightmap to that of other physical features, i.e., norm

map and detrended heightmap, as shown by horizontal lines in Fig. 11. Their EERs are much worse than using the third-highest spatial-frequency subband.